Magneto-optical Bi:YIG films with high figure of merit for non-reciprocal photonics

Takian Fakhrul[*], *Stana Tazlaru, Lukáš Beran, Yan Zhang, Martin Veis, Caroline A. Ross*[*]

T. Fakhrul, Y. Zhang, Prof. C. A. Ross

Department of Materials Science and Engineering

Massachusetts Institute of Technology

Cambridge, MA, 02139, USA

E-mail: takianf@mit.edu ; caross@mit.edu

S. Tazlaru, L. Beran, Prof. M. Veis

Faculty of Mathematics and Physics

Charles University

Ke Karlovu 3, 12116 Prague 2, Czech Republic

Y. Zhang

Engineering Research Center of Electromagnetic Radiation Control Materials

University of Electronic Science and Technology of China

Chengdu 610054, China

This is the author manuscript accepted for publication and has undergone full peer review but has not been through the copyediting, typesetting, pagination and proofreading process, which may lead to differences between this version and the Version of Record. Please cite this article as doi: 10.1002/adom.201900056.

Abstract

Thin film magneto-optical materials are enablers for integrated non-reciprocal photonic devices such as isolators and circulators. Films of polycrystalline bismuth-substituted yttrium iron garnet (Bi:YIG) have been grown on silicon substrates and waveguide devices in which a YIG seedlayer is placed either above or below the active Bi:YIG layer to promote crystallization. The films exhibit a high magneto-optical figure of merit of up to 769 $^{\circ}dB^{-1}$ at 1550 nm wavelength. Growth of single phase Bi:YIG on the sidewalls of waveguides is demonstrated, which can be used in non-reciprocal transverse electric (TE)-mode devices.

1. Introduction

Rapid development of optical fiber communication systems has prompted the growing demand for photonic integrated circuits (PICs) with multiple functions including lasing, modulation, transmission and detection of photons.[1-6] One key function is optical isolation. Optical isolators play a crucial role in PICs by controlling the flow of light, reducing unwanted light reflections between different parts of the circuit and preventing destabilization of the laser source.

Optical isolators as well as circulators are based on non-reciprocal phenomena, most commonly magnetooptical, that break the symmetry between forward and backward propagating light. Discrete isolators rely on Faraday rotation, i.e. a non-reciprocal mode conversion, but in PICs the use of nonreciprocal phase shift (NRPS) in a resonator or interferometer device is preferable to avoid problems caused by the birefringence of optical waveguides. The active material in these isolator devices is commonly a magneto-optical (MO) iron garnet material, in particular yttrium iron garnet (YIG, $Y_3Fe_5O_{12}$) with substituents such as Ce or Bi to increase the MO performance.[5-15]

However, the integration of garnets on a Si (or other semiconductor) platform is challenging due to the incompatible lattice parameters and the thermal expansion mismatch between garnets and common semiconductor substrates.[6-16] Moreover, crystallization of the garnet phase usually requires a high thermal budget. Garnets formed on semiconductor substrates are polycrystalline and exhibit higher optical absorption than single crystal films. Furthermore, impurity phases such as $YFeO_3$, Fe_2O_3 and Bi_2O_3 can form during the crystallization process,[17] which contributes to optical loss. These factors result in inferior optical performance of polycrystalline MO garnet films compared to the bulk garnet material, and a lower figure of merit (FoM), defined as the ratio of the Faraday rotation to the absorption coefficient per length of the material.

Considerable work has been done on growth of garnet films on semiconductors to enable demonstrations of isolators and modulators.[6-16] The first monolithically integrated optical isolator [6]

used 80 nm thick Ce:YIG which was grown by pulsed laser deposition (PLD) on a pre-annealed 20 nm thick YIG seed layer to induce crystallization of the Ce:YIG. A simplified PLD process was introduced by Sun et al.[11] where the YIG seed layer was placed on top of the MO garnet and both layers were crystallized simultaneously by rapid thermal annealing (RTA). This top-seedlayer process places the MO garnet in direct contact with the underlying Si waveguide, maximizing the coupling of light from the waveguide to the MO cladding, but it has only been applied to Ce:YIG. Recently rare-earth garnets have been developed that crystallize on Si and quartz without a seed layer, including sputter-deposited terbium iron garnet (TIG) and Bi-doped TIG (Bi:TIG).[18,19]

Growth of MO materials on the sidewall of the waveguide can enable a wider range of device designs, including isolators for TE (transverse electric) polarization. Integrated semiconductor lasers emit TE-polarized light, and TE mode isolation using NRPS requires placement of the MO material on the sidewall of the waveguide to break left-right symmetry.[18,20,21] However, the NRPS-based integrated optical isolators that have been experimentally demonstrated are made with the MO material on the top or bottom surface of the waveguide, which isolates only the TM (transverse magnetic) polarization.[6-8,11-14] It is therefore essential to establish deposition conditions that yield well-crystallized MO garnet on the sidewalls of waveguides to facilitate TE-mode isolation without requiring additional mode converters.

Ce:YIG is the most commonly used MO material for integrated optical isolators designed to operate at 1550 nm. However, Ce:YIG has an absorption peak from a Ce transition near 1.3 eV with a notable tail extending into the IR, leading to a decreasing FoM as the wavelength is reduced below 1550 nm.[13,22] Bi:YIG lacks this absorption peak, making it favorable for isolators in the lowest dispersion 1300 nm wavelength range,[6,7,13] and bulk Bi:YIG is the material of choice in discrete isolators. Single-crystal Bi:YIG has been extensively characterized.[23-35] Epitaxial Bi:YIG films on $Gd_3Ga_5O_{12}$ (GGG) (111) substrates exhibited a Faraday rotation angle Θ_f proportional to the Bi content.[24] Complete substitution of bismuth in YIG can increase the Faraday rotation by as high as two orders of magnitude at 633 nm wavelength in comparison to YIG.[23, 32, 45] The Bi^{3+} ion has high spin orbit coupling that increases excited state splitting, raising the Faraday rotation.[34] Although polycrystalline Bi:YIG has been grown and characterized,[6, 7, 33, 36-40] its reported FoM is well below that of bulk Bi:YIG and there has been no systematic study of its FoM as a function of composition or deposition parameters.

In this paper we report the growth and optical properties of epitaxial and polycrystalline thin films of Bi-substituted yttrium iron garnet ($Bi_xY_{3-x}Fe_5O_{12}$, Bi:YIG) synthesized using PLD on GGG and Si substrates. The optimum growth conditions for epitaxial films and the effect of growth temperatures and O_2 pressure on the film stoichiometry was studied. The key results are demonstrations of the highest reported FoM of polycrystalline Bi:YIG films; the top-down seedlayer process for Bi:YIG; and the sidewall growth of Bi:YIG. The microstructure and stoichiometry of the films grown on the top surface and on the sidewalls of waveguide structures was compared to address the challenges of developing TE mode optical isolators.

2. Characterization of Bi:YIG/GGG

2.1. Structural Characterization

We first describe the PLD growth, structure and properties of single crystal Bi:YIG films grown on GGG. Bi:YIG films of thickness 30 to 100 nm grew epitaxially on the substrate according to XRD analysis. The high crystalline quality of the epitaxial films is evident from the Laue fringes present in the HRXRD symmetric scans around the Bi:YIG and GGG (400) peaks as shown in Figure 1a. The out-of-plane lattice parameters of $Bi_xY_{3-x}Fe_5O_{12}$ grown from targets with x = 0.8, 1.2 and 1.5 and at 20mTorr oxygen pressure and substrate temperature of 560°C were 12.41 Å, 12.50 Å and 12.56 Å respectively in agreement with previous reports.[23,24,33]

2.2. Effect of Temperature and Oxygen Pressure on Stoichiometry

The effects of substrate temperature (T_s) and oxygen pressure (P_{O_2}) on film composition are shown in Figure 1b and Figure 1c. The cation content of the films was measured by wavelength dispersive spectroscopy and characterized by the Bi:Y ratio and by (Bi+Y)/Fe which is ideally 0.6. Films grown on Si during the same deposition run showed the same cation ratios found in films grown on GGG.

High T_s and/or low P_{O_2} lead to a lower bismuth content whereas low T_s and/or high P_{O_2} result in bismuth-rich films as shown in Figure 1d. This bismuth deficiency at higher T_s is attributed to the volatility of bismuth, and similar behavior has been observed in $BiFeO_3$ films.[41,42] The pressure dependence is related to scattering of the ablated species by the oxygen in the chamber. Fe is lighter than Bi and is scattered more effectively, accounting for the Fe deficiency at higher P_{O_2}. Increasing oxygen pressure also lowered the ratio of Fe to Y. As a result, for constant temperature the (Bi+Y):Fe ratio is much less than 0.6 at lower P_{O_2} but increases with P_{O_2} as shown in Figure 1d.

The (Bi+Y):Fe ratio was close to the stoichiometric ratio of 0.6 at growth temperatures of 520-600°C at P_{O_2} of 20 mTorr (Figure 1d) and XRD analysis confirms formation of single phase garnet in this temperature range. While a single phase garnet without secondary phases was formed at all oxygen pressures between 10-100mTorr, the Bi-rich films at higher oxygen pressures have improved magneto-optical characteristics (Figure 2d).

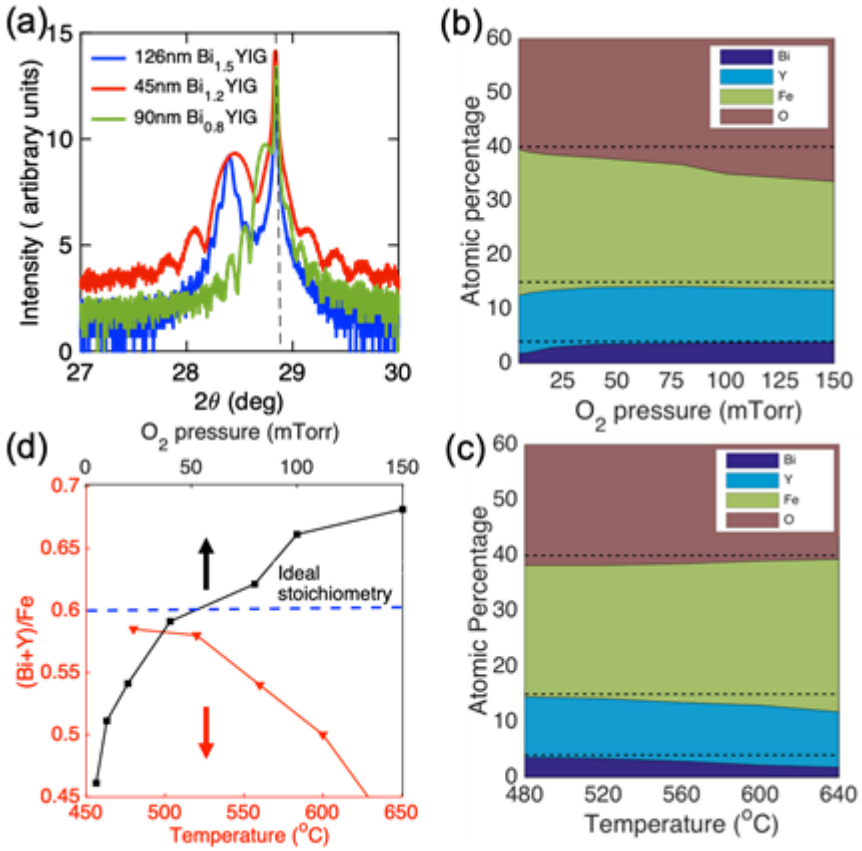

Figure 1. (a) HRXRD ω −2Θ scans around the Bi:YIG (400) and GGG (400) peaks for films grown at 560 °C and 100mTorr pressure. Dashed line indicates the (400) peak of bulk GGG. (b) Effect of oxygen pressure on composition of films grown from a target composition of $Bi_{0.8}Y_{2.2}Fe_5O_{12}$ at 560 °C, repetition rate 10 Hz and laser fluence of 2 J/cm^2. (c) Effect of substrate temperature on composition of films grown from target composition of $Bi_{0.8}Y_{2.2}Fe_5O_{12}$ at 20 mTorr, repetition 10 Hz and laser fluence of 2 J/cm^2. (d) The corresponding (Bi+Y)/Fe ratios in (b) and (c) plotted as a function of temperature (red) and O_2 pressure (black).

Table 1. Growth conditions and stoichiometry of garnet films on GGG and Si.

Sample	Substrate	Target	P_{O2} (mTorr)	Temperature (^oC)	Film Thickness (nm)	Bi:Y:Fe
G1	GGG	$Bi_{1.2}Y_{1.8}Fe_5O_{12}$	150	520	104	1:1.6:3.6
G2			100		110	0.9: 2:4
G3			20		130	0.65:2.2:4.6
G4		$Bi_{1.5}Y_{1.5}Fe_5O_{12}$	100	560	126	1.4:1:4.2
G5		$Bi_{1.2}Y_{1.8}Fe_5O_{12}$	150	560	75	1.1:1.4:4
G6		$Bi_{0.8}Y_{2.2}Fe_5O_{12}$	100	560	90	0.7:1.9:4
S1	Si	$Bi_{0.8}Y_{2.2}Fe_5O_{12}$	100	560	YIG(37)/BiYIG(88)/Si	
S2		$Bi_{1.2}Y_{1.8}Fe_5O_{12}$	100	560	YIG(40)/BiYIG(80)/Si	
S3		$Bi_{1.5}Y_{1.5}Fe_5O_{12}$	100	640	YIG(50)/BiYIG(90)/Si	
S4		$Bi_{0.8}Y_{2.2}Fe_5O_{12}$	100	560	BiYIG(85)/YIG(20)/Si	
S5		$Bi_{1.2}Y_{1.8}Fe_5O_{12}$	100	560	BiYIG(90)/YIG(25)/Si	
S6		$Bi_{1.5}Y_{1.5}Fe_5O_{12}$	100	600	BiYIG(100)/YIG(40)/Si	

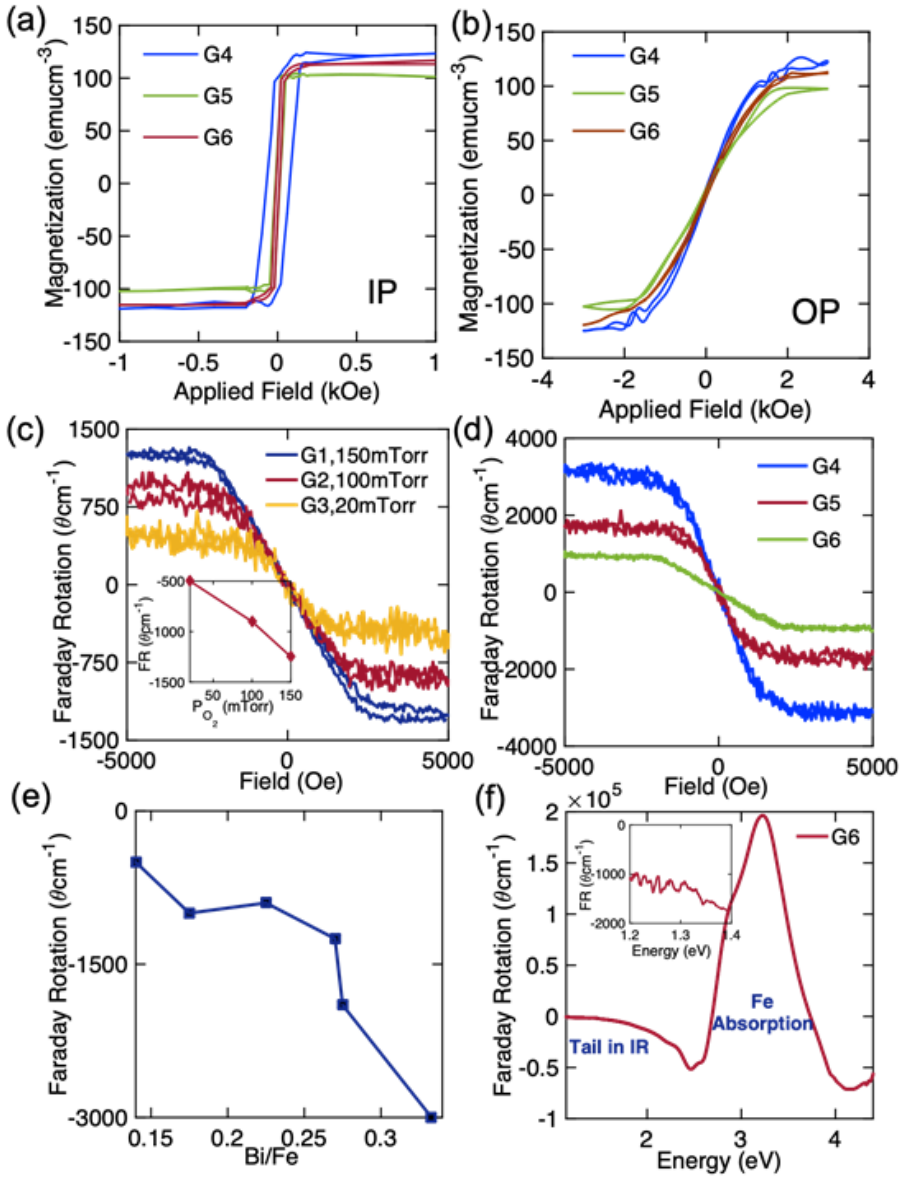

Figure 2. (a) In-plane (IP) and (b) out-of-plane (OP) hysteresis loops for epitaxial films grown from targets of varying bismuth content. (c) Out-of plane Faraday rotation hysteresis loops at 1550 nm for films grown at 520°C, 1.9J/cm² at various oxygen pressures from a $Bi_{1.2}Y_{1.8}Fe_5O_{12}$ target. (d) Out-of plane Faraday rotation hysteresis loops at 1550 nm for epitaxial Bi:YIG films made from $Bi_{0.8}Y_{2.2}Fe_5O_{12}$, $Bi_{1.2}Y_{1.8}Fe_5O_{12}$ and *$Bi_{1.5}Y_{1.5}Fe_5O_{12}$ targets*. (e) *Faraday rotation versus Bi/Fe ratio of epitaxial films. (f) Faraday rotation spectrum of an epitaxial film made from a $Bi_{0.8}Y_{2.2}Fe_5O_{12}$ target.*

2.3. Magnetic and Magneto-optical Characterization

The single crystal films grown on GGG have a saturation magnetization of approximately 120 cmu cm^{-3} (Figure 2a and Figure 2b), similar to previous reports,[6,7] and Faraday rotation up to $3000^{o}\,cm^{-1}$ at 1550 nm wavelength, Figure 2c. The Faraday rotation increased linearly with the bismuth content as reported previously.[24] Hence, the Faraday rotation can be increased by using a target with higher Bi content or by depositing at a higher oxygen pressure to enhance Bi incorporation into the films. In Figure 2f, the Faraday rotation versus wavelength for Bi:YIG/GGG is typical of bulk Bi:YIG with absorption in the visible-ultra violet region due to Fe transitions, and an absorption tail extending into the IR.[34,35, 44-46]

3. Characterization of Bi:YIG/Si

3.1. Structural Characterization, Surface Morphology and Crystal Quality

We now discuss the properties of Bi:YIG films grown on Si substrates by PLD from the same three targets of composition $Bi_{0.8}Y_{2.2}Fe_5O_{12}$, $Bi_{1.2}Y_{1.8}Fe_5O_{12}$ and $Bi_{1.5}Y_{1.5}Fe_5O_{12}$. Annealing of single layer Bi:YIG films did not produce a garnet phase, but inclusion of a YIG seed layer led to crystallization into garnet as shown previously for Ce:YIG.[6,7] Bilayers consisting of Bi:YIG with a YIG seed layer below or above the Bi:YIG are referred to as bottom-up or top-down, respectively. Layer thicknesses are given in Table 1.

Figure 3b shows the XRD pattern for bottom-up and top-down crystallized bilayers after RTA at 800 °C for 5 min. While the bottom-up crystallized films form no secondary phases the top-down crystallized films contain secondary phases in the form of Bi_2O_3 and Fe_2O_3. We suggest that in the top-down crystallization process the escape of volatile Bi during annealing is limited by the capping YIG seed layer and the excess Bi forms the secondary Bi_2O_3 phases. The introduction of an additional annealing step in the PLD chamber after the growth of the Bi:YIG layer but before the YIG was deposited allows part of the Bi to escape and prevents the formation of secondary phases as shown in Figure 3b. The excess Bi in the top-down bilayers was alternatively avoided by co-depositing iron oxide from a separate target during growth. However, this process resulted in a slight excess of Fe_2O_3 in the film as shown in Figure 3b. XRD data for a broad range of angles ($2\theta = 20^{o}$ to 50^{o}) for the polycrystalline films further confirms the presence of secondary phases only in the top-down crystallized Bi:YIG films that were not PLD annealed or co-deposited with Fe_2O_3 as shown in Figure S1. The SEM and AFM surface morphology of the bilayer films of YIG/Bi:YIG/Si and Bi:YIG/YIG/Si are shown in Figure 3c and Figure 3d. For the YIG/Bi:YIG/Si, the grain size at the top surface is on the order of 5 μm, whereas in Bi:YIG/YIG/Si the grain size is on the order of 2 μm.

Figure 4a shows the cross-sectional SEM image of top-down crystallized YIG (50nm)/Bi:YIG (150nm)/substrate grown on a waveguide of a TE mode optical test device. TE-mode optical isolation

requires symmetry breaking that is transverse to the waveguide and therefore sidewall garnet growth is necessary.[47] The garnet covers both the top surface and the sidewalls, but the layer on the sidewall of the trench is thinner than the layer on the flat surface of the device. Moreover, the sidewall coverage of garnet on either side of the trench is significantly different because the trench was not placed directly above the plume during deposition. By rotating the substrate during deposition a much more uniform side wall coverage on both sides of the trench is obtained as shown in the cross-sectional TEM image of YIG (100nm)/Bi:YIG(100nm)/substrate in Figure 4b. Figure 4a also confirms that the Bi:YIG layer shows internal contrast, presumably from grain boundaries, and has a smaller grain size than the YIG capping layer.

A bright-field TEM cross-sectional image of YIG/Bi:YIG film on amorphous SiO_2 is shown in Figure 4c. The Au and Pt layers were added during sample preparation prior to cutting the sample using the FIB. A high-resolution (HR) TEM image of the interface between the YIG and the Bi:YIG layer is shown in Figure 4d. Figure 4e and Figure 4f show selected area diffraction (SAD) pattern of the garnet grown on the flat surface of the device taken along the $[0\bar{1}\bar{1}]$ zone axis and of sidewall garnet along the $[\bar{1}11]$ zone using apertures indicated in Figure 4b in blue and red respectively. The SAD patterns show diffraction spots consistent with the garnet structure, and their spacing yielded interplanar spacings of d_{321}= 3.34 Å, d_{422}= 2.55 Å, d_{400}= 3.10Å close to the lattice spacings from XRD. (d_{321}= 3.31 Å, d_{422}= 2.52 Å, d_{400}= 3.09Å).

Figure S2 shows the elemental mapping of Fe, Y, O, Bi and Au in the top-down YIG/Bi:YIG/Si from the scanning transmission electron microscope sample together with a bright field TEM image. The distribution of Fe and Y is uniform throughout the YIG and Bi:YIG layers. However, the Fe distribution on the sidewall includes Fe-rich regions as shown in Figure S3. The Bi map suggests interdiffusion of Bi into the YIG layer. The false signal in the Bi map at the top of the Bi:YIG film is due to an overlap of the Bi Mα peak with the Au Lα peak.

3.2. Magnetic and Magneto-optical Characterization

The polycrystalline films grown with both top and bottom seed layers on planar Si substrates had bulk-like magnetic moment (Figure 5a and Figure 5b) and Faraday rotation up to $2000^{o}\,cm^{-1}$ at 1550 nm was achieved for top-down crystallized films grown from the $Bi_{1.5}Y_{1.5}Fe_5O_{12}$ target (Figure 5c). The high Faraday rotation of the films S3 and S6 is attributed to the increased Bi content from the $Bi_{1.5}Y_{1.5}Fe_5O_{12}$ target.[24,34,35,45] For all the polycrystalline films the Faraday rotation was averaged over the entire bilayer thickness, i.e. including the YIG contribution, and was comparable for both top-down and bottom-up films grown from the same target composition as shown in the inset in Figure 5d.

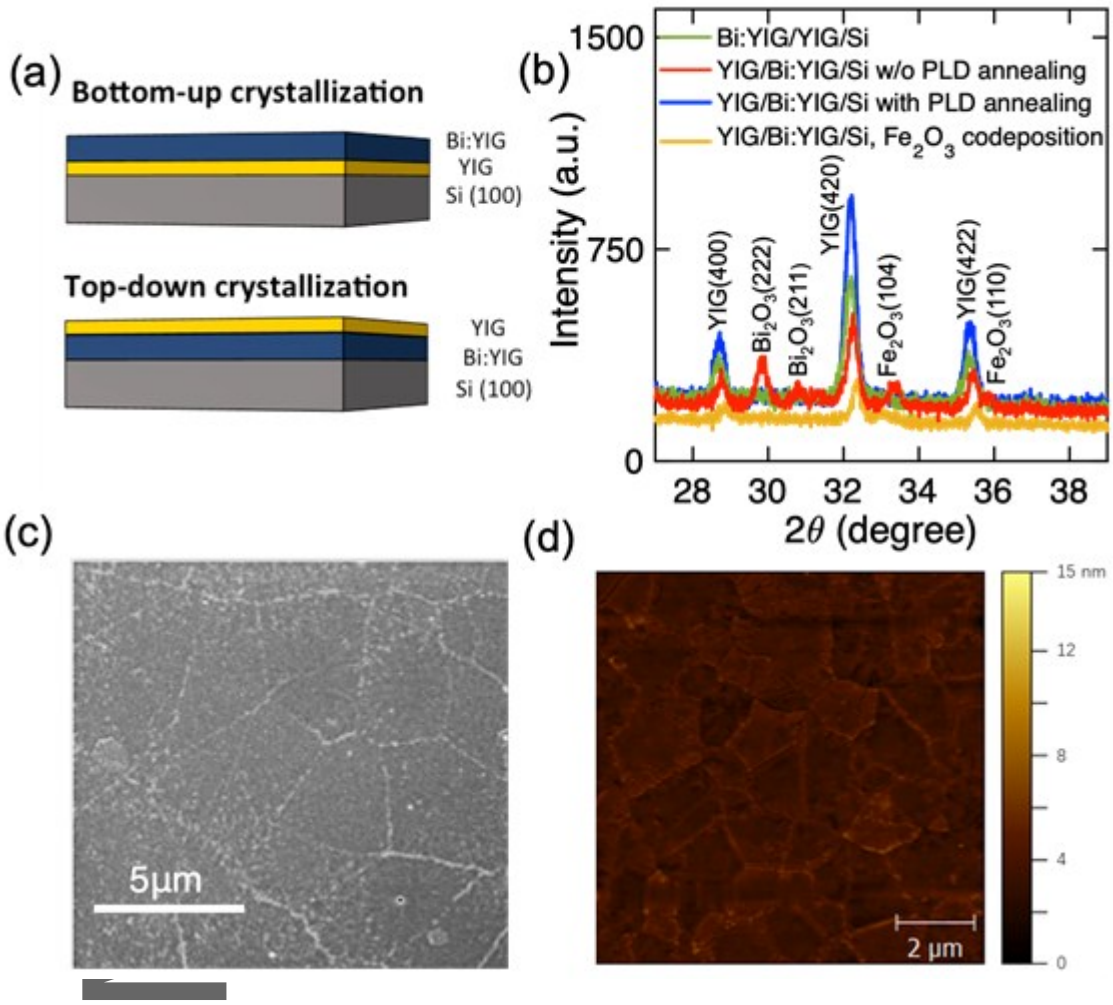

Figure 3. (a) Schematic of bottom-up and top-down crystallized films. (b) XRD ω−2θ scans for polycrystalline Bi:YIG films on silicon after RTA. (c) SEM image of crystallized top surface of YIG/Bi:YIG/Si film after rapid thermal annealing. (d) AFM image of Bi:YIG/YIG/Si film after rapid thermal annealing, with color scale showing the height.

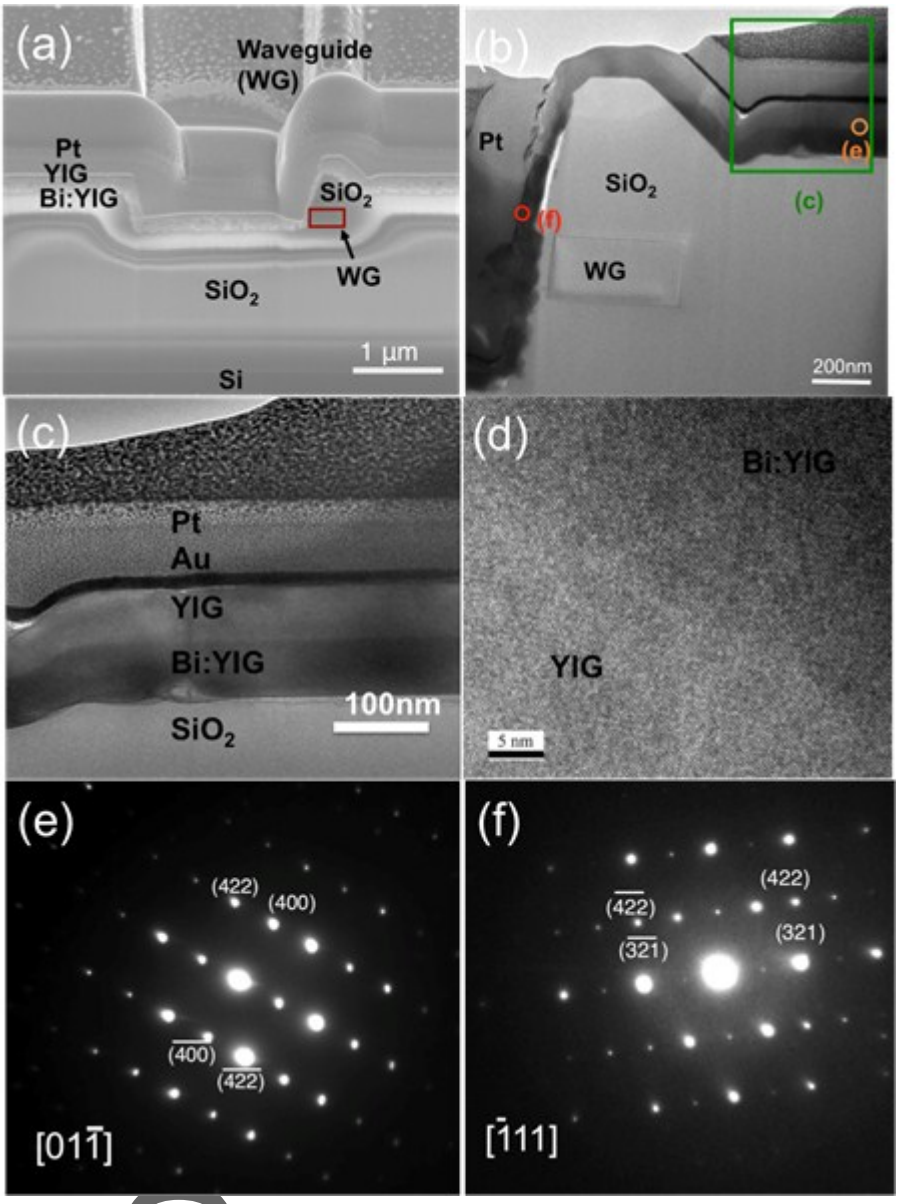

Figures 4(a) and (b) show the cross-sectional SEM and TEM images of top-down crystallized Bi:YIG film grown on a waveguide of an optical test device. In (a) the waveguide cross-section is highlighted in red. (c) Bright-field TEM cross-sectional images of bilayer film. (d) High resolution TEM images of the interface between the YIG and Bi:YIG layer. (e) Selected area diffraction (SAD) pattern taken along the [01$\bar{1}$] *zone axis of the planar surface of the device with the aperture placed at the location indicated in orange in (b). (f) SAD pattern taken along* the [$\bar{1}$11] *zone axis at the location indicated in red in (b).*

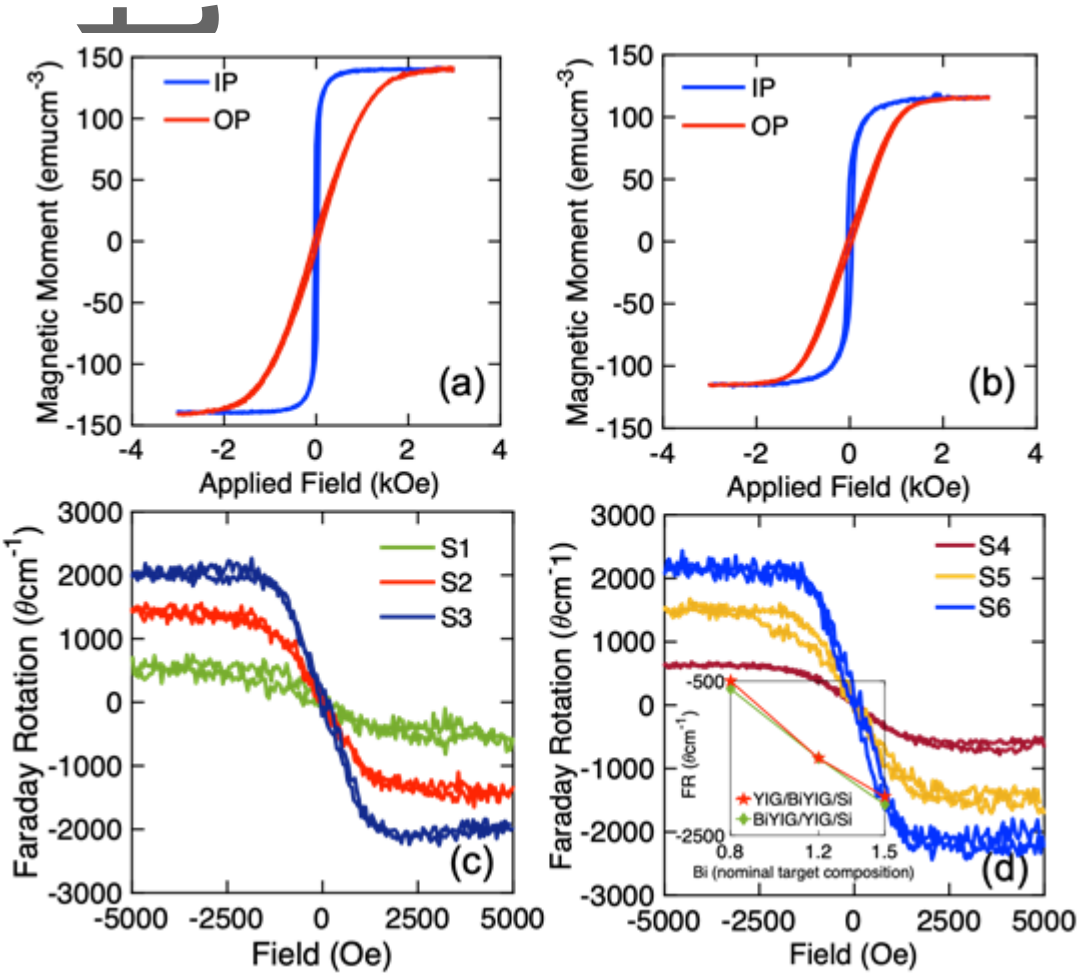

Figure 5. In-plane (IP) and Out-of-plane (OP) hysteresis loops of films on Si after RTA (a) bottom-up crystallized film from $Bi_{1.2}Y_{1.8}Fe_5O_{12}$ target (b) top-down crystallized film from $Bi_{1.5}Y_{1.5}Fe_5O_{12}$ target. Out-of plane Faraday rotation hysteresis loops at 1550 nm wavelength of (c) top-down YIG/Bi:YIG and (d) bottom-up YIG/Bi:YIG films grown from target compositions of $Bi_{0.8}Y_{2.2}Fe_5O_{12}$, $Bi_{1.2}Y_{1.8}Fe_5O_{12}$ and $Bi_{1.5}Y_{1.5}Fe_5O_{12}$. Inset in (d) shows Faraday rotation versus nominal target composition for bottom-up and top-down films.

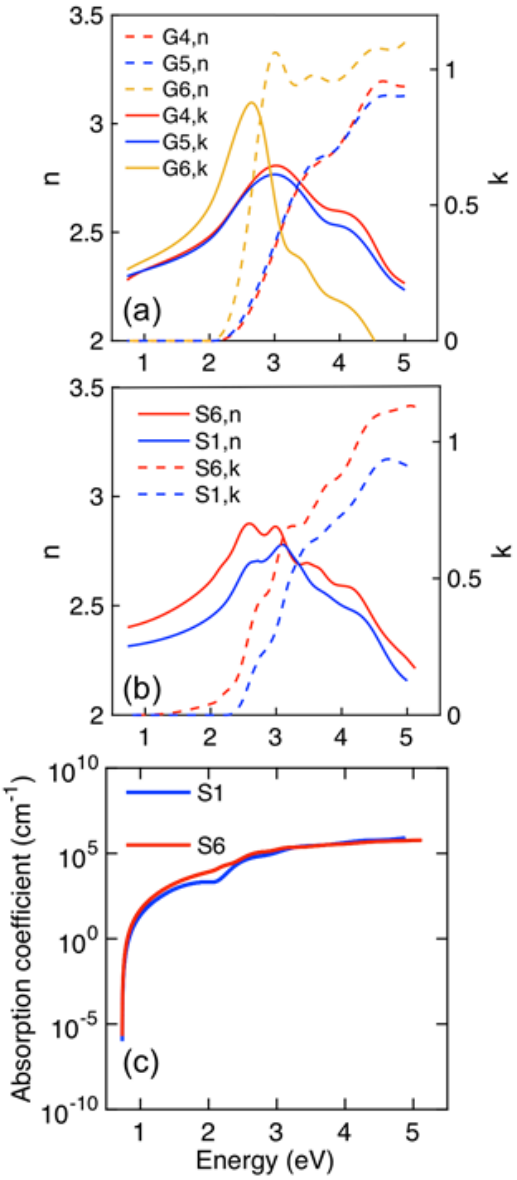

Figure 6. *Refractive index (n) and extinction coefficient (k) spectra of (a) Bi:YIG/GGG (b) Bi:YIG/YIG/Si and YIG/Bi:YIG/Si films characterized by spectroscopic ellipsometry. (c) Spectral dependence of absorption coefficient of Bi:YIG/YIG/Si and YIG/Bi:YIG/Si films.*

4. Optical Characterization

Experimental data measured by spectroscopic ellipsometer were fitted using a model structure of (a) thin Bi:YIG layer on GGG substrate, or (b) YIG/Bi:YIG layer on oxidized Si substrate. The optical parameters of GGG and YIG were obtained from separate measurements on bare GGG substrate and on a 90 nm thick YIG layer on GGG substrate. Kramers-Kronig consistency of the results was ensured by the dispersion model used.

Spectral dependences of the real, n, and imaginary, k, part of the complex refractive index are shown in Figure 6a and 6b. The spectral behavior is typical for ferrimagnetic garnets.[13,34,43,45,46] Figure 6b clearly shows an increase in the absorption below the absorption edge with increasing Bi content, as was previously reported.[34] Using the results in Figure 6b we have calculated spectral dependence of the absorption coefficient of the samples grown on Si substrates. The resulting spectra are displayed in Figure 6c.

The absorption coefficient falls dramatically in the IR region on moving away from the optical absorption edge. The films exhibit the highest values of FoM at 1550 nm reported for polycrystalline Bi:YIG films to date, as shown in Table 2. The lower bound of the FoM was 397 and 769° dB^{-1} at 1550 nm (E = 0.8 eV) for sample S1 and S6 from Table 1 respectively. These FoM values are more than an order of magnitude higher than previous reports for polycrystalline Ce:YIG films.[6,12]

5. Conclusion

In conclusion, polycrystalline YIG/Bi:YIG films were grown on Si in both bottom-up and top-down configuration using a single-step PLD method in which the YIG layer provides a template for Bi:YIG crystallization. Top-down YIG/Bi:YIG was demonstrated for the first time, crystallizing on both planar substrates and on sidewall features, and its Faraday rotation was as high as 2000^{o} cm^{-1} at 1500 nm. The top-down process allows the MO Bi:YIG layer to be placed in direct contact with an underlying waveguide which is expected to increase optical coupling into the Bi:YIG and improve the performance of integrated optical isolators. The FoM reported for both the top down and bottom-up crystallized films at 1550 nm are more than one order of magnitude higher than previous reported FoM values for polycrystalline MO garnets suggesting Bi:YIG as a material for non-reciprocal integrated photonics with enhanced performance.

Table 2. Comparison of MO Figure-of-merit values for polycrystalline garnets on non-garnet substrates, single crystalline garnets on garnet substrates and bulk garnets at λ = 1550 nm.

MO material and substrate	MO FoM [°dB^{-1}]	Growth Method	Optical Loss [dB.cm^{-1}]	Reference
$Y_{2.82}Ce_{0.18}Fe_5O_{12}$ (no substrate, bulk crystal)	1420	Traveling solvent floating zone	0.52	22
Single crystalline epitaxial Ce:YIG on GGG (111) substrate	943	PLD	6	13
Polycrystalline CeYIG on YIG on Si substrate	38	PLD	29	12
Ce:YIG on Si	21.8	PLD	58	6
YIG/$Bi_{0.8}$YIG/Si	397	PLD	1.26	This work
$Bi_{1.5}$YIG/YIG/Si	769	PLD	2.6	This work

6. Experimental Section

The Bi:YIG and YIG films were deposited by PLD on double-side polished silicon (100) and GGG(100) substrates using a 248nm wavelength KrF excimer laser (Coherent, COMPex Pro 205). The $Bi_xY_{3-x}Fe_5O_{12}$ (x = 0.8, 1.2, 1.5) and $Y_3Fe_5O_{12}$ targets were prepared by sintering of mixed oxide powders.[11] The chamber was pumped to 5×10^{-6} Torr base pressure prior to introducing oxygen and depositing the films. The laser repetition rate was 10 Hz, the laser fluence was ~2 J/cm^2, and the target-substrate distance was 6 cm. A range of different substrate temperatures (480-650^{o}C) and O_2 pressures (5-100mTorr) were used. The films grown on Si consisted of YIG 30 nm/Bi:YIG 100 nm/Si and Bi:YIG 100 nm/YIG 80 nm/Si, and underwent rapid thermal annealing (RTA, Modular Process Tech, RTP-600S) at 800 °C for 5 min. Crystallization of the Bi:YIG during RTA is facilitated by the YIG layer on top of or at the bottom of the stack as shown in Figure 3a.

Phase analysis and lattice parameters of the epitaxial films were characterized by Bruker D8 Discover HRXRD. For the polycrystalline films, θ−2ω diffraction data were collected on a PANalytical X'pert Pro MPD diffractometer. The thickness was measured by surface profilometry on a KLA-Tencor P-16+ stylus profiler having measurement error of less than 5%. Atomic force microscopy was carried out using Veeco Metrology Nanoscope IV Scanned Probe Microscope Controller with Dimension 3100 SPM. The epitaxial film compositions were measured by wavelength dispersive spectroscopy

(WDS) using a JEOL-JXA-8200 Superprobe. Cross-section samples for TEM were prepared using focused ion beam (FEI- 600) and then imaged on a JEOL 2010F field-emission TEM. STEM EDX was used to carry out the elemental mapping in the films. Room temperature magnetic properties were characterized by vibrating sample magnetometry (VSM) using an ADE Technologies VSM Model 1660. Spectroscopic ellipsometry was performed on a J.A. Woollam RC2 ellipsometer for three light incident angles ranging from 55˚ to 65˚. The experimental data were processed using proprietary software CompleteEase by J.A. Woollam. Faraday rotation hysteresis loops were measured at 1550 nm with magnetic field and light propagation perpendicular to the films.

Acknowledgements

The support of National Science Foundation award ECCS 1607865 is gratefully acknowledged. This work made use of Shared Experimental Facilities supported in part by the MRSEC Program of the NSF under award number DMR - 1419807.

Conflict of Interest

The authors declare no conflict of interest.

Keywords

Magneto-optical garnet, optical isolators, bismuth iron garnet, monolithic integration, magneto-optics, sidewall, thin film

References

[1] D. Thomson, A. Zilkie, J. E. Bowers, T. Komljenovic, G. T. Reed, L. Vivien, D. Marris-Morini, E. Cassan, L. Virot, J. M. Fédéli, J. M. Hartmann, J. H. Schmid, D.-X. Xu, F. Boeuf, P. O. Brien, G. Z. Mashanovich, M. Nedeljkovic, *J. Opt*. **2016**, *18*, 073003.

[2] V. R. Almeida, C.A. Barrios, R. R Panepucci, M. Lipson, *Nature* **2004** , 431,1081.

[3] R. Soref, in Proc. *SPIE 5730*, Optoelectronic Integration on Silicon II, San Jose, California, **2005**.

[4] L. Fan, J. Wang, L. T. Varghese, H. Shen, B. Niu, Y. Xuan, A. M Weiner, M. Qi, *Science* **2012**, *335*, 447.

[5] D. Huang, P. Pintus, J. E. Bowers, *Opt. Mater. Express* ***2018****, 8*, 2471

[6] L. Bi, J. Hu, P. Jiang, D. H. Kim, G. F. Dionne, L. C. Kimerling, C. A. Ross, *Nat. Photonics* **2011**, *5*, 758.

[7] L. Bi, J. Hu, P. Jiang, H. S. Kim, D. H. Kim, M. C. Onbasli, G. F. Dionne, C. A. Ross, *Materials* ***2013****,* 6, 5094.

[8] Q. Du, T. Fakhrul, Y. Zhang, J. Hu, C. A. Ross. 2018, *MRS Bull.* **2018**, *43*, 413

[9] H. Yokoi, T. Mizumoto, Y. Shoji, *Appl. Opt.* **2003**, *42*, 6605.

[10] K. Srinivasan, B. J. Stadler, *Opt. Mater. Express* **2018**, *8*, 3307.

[11] X. Y. Sun, Q. Du, T. Goto, M. C. Onbasli, D. H. Kim, N. M. Aimon, J. Hu, C.A. Ross, *ACS Photonics* **2015**, *2*, 856.

[12] T. Goto, M. C. Onbaşlı, C. A. Ross. **2012.** *Opt. Exp*ress 2012, *20*, 28507.

[13] M.C. Onbasli, L. Beran, M. Zahradník, M. Kučera, R. Antoš, J. Mistrík, G. F. Dionne, M. Veis, C. A. Ross, *Sci. Rep.* **2016**, *6*, 23640.

[14] T. Mizumoto, Y. Shoji, R. Takei, *Materials* **2012,** 5, 985.

[15] B. J. Stadler, T, Mizumoto, *IEEE Photonics J.* **2014**, *6*, 1.

[16] Q. Du, C. Wang, Y. Zhang, Y. Zhang, T. Fakhrul, W. Zhang, C. Goncalves, C. Blanco, K. Richardson, L. Deng, C.A. Ross, L. Bi, J. Hu, *ACS Photonics* **2018**, *5* , 5010.

[17] N. Kumar, D. S. Misra, N. Venkataramani, S. Prasad, R. Krishnan, *J. Magn. Magn. Mater*. **2004**, *272*, E899.

[18] P. Dulal, A. D. Block, T. E. Gage, H.A Haldren, S. Y. Sung, D. C. Hutchings, B. J. Stadler, *ACS Photonics* **2016**, *3*, 1818.

[19] C. Zhang, P. Dulal, B. J. Stadler, D.C. Hutchings, *Sci. Rep.* **2017**, *7*, 5820.

[20] Y. Shoji, T. Mizumoto, *Sci. Technol. Adv. Mater*. **2014**, *15*, 014602.

[21] P. Pintus, F. D. Pasquale, J. E Bowers, *Opt. Lett*. **2011**, *36*, 4599.

[22] S. Higuchi, S. Takekawa, S. K. Kitamura, *Jpn. J. Appl. Phys.* **1999**, *38*, 4122.

[23] T. Tepper, C.A. Ross, *J. Cryst. Growth* **2003**, *255*, 324.

[24] M. Y. Chern, J. S. Liaw, *Jpn. J. Appl. Phys.* **1997**, *36*, 1049.

[25] L. Soumah, N. Beaulieu, L. Qassym, C. Carrétéro, E. Jacquet, R. Lebourgeois, J. B. Youssef, P. Bortolotti, V. Cros, A. Anane, *Nat. Commun.* ***2018****, 9*, 3355.

[26] A. Hasanpour, M. Mozaffari, J. Amighian, H. Richert, A. Lorenz, M. Lindner, P. Görnert, H. Heegn, *J. Magn. Magn. Mater*. **2007**, *317*, 41.

[27] J. M. Robertson, S. Wittekoek, T. J. Popma, P. F. Bongers, *Appl. Phys.* **1973**, *2*, 219.

[28] S. Leitenmeier, T. Körner, J. Griesbauer, M. Herbort, A. Heinrich, B. Stritzker, *J. Cryst. Growth* **2008**, *310*, 5392.

[29] S. Kahl, A. M. Grishin, *Appl. Phys. Lett*. **2004**, *84*, 1438.

[30] G. Siegel, M.C. Prestgard, S. Teng, A. Tiwari, *Sci. Rep.* **2014**, *4*, 4429.

[31] R. Lux, A. Heinrich, S. Leitenmeier, T. Körner, M. Herbort, B. Stritzker, *J. Appl. Phys.* **2006**, *100*, 113511.

[32] N. Adachi, V. P. Denysenkov, S. I. Khartsev, A. M Grishin, T. Okuda, *J. Appl. Phys.* **2000**, *88*,2734.

[33] M. Veis, E. Lišková, R. Antoš, Š. Višňovský, N. Kumar, D. S. Misra, N. Venkataramani, S. Prasad, R. Krishnan, *Thin Solid Films* **2011**, *519*, 8041.

[34] S. Wittekoek, T. J. Popma, J. M. Robertson, P.F. Bongers, *Phys. Rev. B* **1975**, *12*, 2777.

[35] M. Y. Chern, F. Y. Lo, D. R. Liu, K. Yang, J. S. Liaw, *Jpn. J. Appl. Phys.* **1999**, *38*, 6687.

[36] M. Inoue, R. Fujikawa, A. Baryshev, A. Khanikaev, P. B. Lim, H. Uchida, O. Aktsipetrov, A. Fedyanin, T. Murzina, A. Granovsky, *J. Phys. D: Appl. Phys.* **2006**, *39*, R151.

[37] T. Körner, A. Heinrich, M. Weckerle, P. Roocks, B. Stritzker, *J. Appl. Phys.* **2008**, *103*, 07B337.

[38] A.D. Block, P. Dulal, B.J. Stadler, N.C. Seaton, *IEEE Photonics J.* **2014**, *6*,1.

[39] S. Geller, H. J. Williams, G. P. Espinosa, R.C. Sherwood, M.A. Gilleo, *Appl. Phys. Lett.* **1963**, *3*, 21.

[40] K. Matsumoto, K. Yamaguchi, T. Fujii, A. Ueno, *J. Appl. Phys.* **1991**, *69*, 5918.

[41] L. Bi, A. R. Taussig, H. S. Kim, L. Wang, G.F. Dionne, D. Bono, K. Persson, G. Ceder, C.A. Ross, *Phys. Rev. B* **2008**, *78*, 104106.

[42] H. Béa, M. Bibes, S. Fusil, K. Bouzehouane, E. Jacquet, K. Rode, P. Bencok, P. A. Barthélémy, *Phys. Rev. B* **2006**,*74*,020101.

[43] G.B. Scott, D. Lacklison, *IEEE Trans. Magn.* **1976**, *12*, 292.

[44] H. L. Gall, M. Guillot, A. Marchand, Y. Nomi, M. Artinian, J. M. Desvignes, *J. Magn. Soc. Jpn.* **1987**, *11*, S1_235.

[45] P. Hansen, J. P. Krumme, *Thin solid films* **1984**, *114*, 69.

[46] G.F. Dionne, G.A. Allen, *J. Appl. Phys.* **1993**, *73*, 6127.

[47] P. Pintus, F. D. Pasquale, J. E Bowers, *Opt. Express* **2013**, *21*, 5041.

Table of Contents

This article presents developments in the integration of magneto-optical (MO) materials into photonic integrated circuits. The first successful demonstration of top-down crystallized polycrystalline Bi:YIG/YIG films on silicon is shown. The figures of merit of the films at 1550 nm are more than one order of magnitude higher than previous reported values for polycrystalline MO garnets. Sidewall growth of garnets, essential for TE-mode isolators, is also demonstrated.

Keywords: Magneto-optical, optical isolator, figure of merit, sidewall growth